Author/s:
Ding, Y;Metha, A;Bedggood, P

Title:
Red Blood Cell Distribution and Volume Changes at Capillary Junctions in the Living Human Retina

Date:
2025-11-01

Citation:
Ding, Y., Metha, A. & Bedggood, P. (2025). Red Blood Cell Distribution and Volume Changes at Capillary Junctions in the Living Human Retina. Investigative Ophthalmology and Visual Science, 66 (14), pp.65-. https://doi.org/10.1167/iovs.66.14.65.

Persistent Link:
https://hdl.handle.net/11343/368003

Red Blood Cell Distribution and Volume Changes at Capillary Junctions in the Living Human Retina

Yifu Ding, Andrew Metha, and Phillip Bedggood

Department of Optometry and Vision Sciences, University of Melbourne, Melbourne, Australia

Correspondence: Yifu Ding, Department of Optometry and Vision Sciences, The University of Melbourne, Parkville, VIC 3010, Australia; yifuding@unimelb.edu.au.

Received: March 21, 2025
Accepted: November 3, 2025
Published: November 26, 2025

Citation: Ding Y, Metha A, Bedggood P. Red blood cell distribution and volume changes at capillary junctions in the living human retina. *Invest Ophthalmol Vis Sci.* 2025;66(14):65. https://doi.org/10.1167/iovs.66.14.65

Purpose. To characterize red blood cell (RBC) distribution and associated changes in cell size at capillary junctions in the human neural retina.

Methods. Cell-resolved blood flow across 60 capillary junctions in the retina of 6 healthy human subjects was measured, using flood-illumination adaptive optics at 200 to 400 fps. Several empirical RBC partitioning models, including a widely used model developed by Pries et al., were compared for predictive accuracy.

Results. We provide updated Pries model coefficients to suit human retinal capillaries. We also propose a simpler linear model that predicts RBC flow distribution based solely on the share of blood flow received by a branch, without reference to the main vessel. Cell size analysis revealed that the average RBC volume in branch vessels was 5.5% lower than in the main vessel ($P < 0.05$). The reduction in cell volume accompanied a 2.3 µm increase in inter-cell spacing ($P < 10^{-4}$) and a 3.0% decrease in hematocrit ($P < 10^{-4}$). These findings support the hypothesis of a net transfer of water from RBCs to plasma as they pass through narrower capillary branches, with potential reabsorption by the time cells enter wider collecting capillaries.

Conclusions. This study provides the first noninvasive in vivo characterization of RBC partitioning behavior at capillary junctions in the living human retina. The subtle fluid exchange between cells and plasma may play a role in optimizing oxygen delivery to support immediate metabolic needs.

Keywords: cell partitioning, capillary bifurcation, microcirculation

Red blood cells (RBCs) travel through a network of vessels that progressively narrow into capillaries, where they exchange gases and metabolites with tissue. Within the microvascular network, the distribution of RBCs is highly heterogeneous, such that vessels of similar branch order and lumen size can exhibit significant variations in the number of cells they receive. This heterogeneity is particularly pronounced in neural tissues with high metabolic demands, such as the brain and retina,[1–3] where branch-specific regulation of capillary flow tailors the oxygen supply to the activities of local neurons.[4–6] Ultimately, the distribution of RBCs occurs at diverging and converging junctions that interconnect capillary segments. Characterizing this process is important for advancing our understanding of tissue oxygenation and for detecting early disruptions in RBC delivery that may precede clinically evident structural changes in microvascular disease. Despite its physiological importance, the RBC partitioning pattern at capillary junctions is not well defined because of technical challenges of resolving blood flow at cellular scale. For the same reason, little is known about the morphological adaptations RBCs make as they traverse these junctions.

To understand the complexities of RBC partitioning at the capillary level, it is useful to first consider how RBCs behave in larger vessels. In vessels with a lumen diameter greater than 1 mm, such as the ophthalmic artery, the influence of RBC size is negligible, and blood behaves as a homogeneous fluid.[7] At this scale, RBC distribution at vascular bifurcations simply follows gross flow distribution. However, when vessel diameters decrease below approximately 300 µm, RBCs migrate toward the center of the vessel, leaving a cell-free plasma layer (CFL) next to the vessel wall.[8,9] Because RBCs cluster in the vessel core, the partitioning at microvascular junctions may no longer reflect gross flow proportions.

To date, the most commonly referred to empirical model describing the distribution of RBC flow in the microvasculature was developed by Pries et al.,[10–12] who studied 65 arteriolar bifurcations in rat mesentery, with vessels ranging from approximately 10 to 30 µm in diameter.[10] Their model predicts that the branch vessel of the arteriolar junction receiving a larger share of blood flow will be enriched with an even higher fraction of RBCs. This skewed partitioning behavior provides a solid explanation for the heterogeneous RBC distribution in the microvasculature. However, the applicability of the Pries model to capillaries with lumen diameters smaller than the undeformed size of an RBC (i.e., ~8 µm), remains uncertain.[13] In these narrow vessels, the CFL, which is a fundamental factor in the Pries model, thins into a lubricating film as RBCs almost fill up the entire vascular lumen.[14] Indeed, the narrow luminal space requires RBCs to deform significantly from their stress-free biconcave shape as they travel. As such, a single-file flow develops, with RBCs alternating with plasma gaps.[8]

Recent three-dimensional (3D) capillary flow simulations have highlighted several factors that can cause cell partitioning behavior in capillaries to deviate from Pries's predictions. For instance, vessel curvature may influence RBC distribution across the vessel cross-section, with deformable cells tending to lateralize toward the side of higher curvature as they travel.[15,16] In addition, RBCs straddling around the apex of capillary bifurcations can temporarily obstruct downstream branches, causing fluctuations in cell partitioning patterns.[17,18] These computational flow models have significantly advanced our understanding of capillary flow dynamics; however, they are not without limitations. Model assumptions such as non-pulsatile flow, uniform cell sizes, and non-stretchable vessel walls all deviate from physiological norms. Furthermore, as these simulations grow more complex with additional variables, their clinical adoption becomes more challenging.

In contrast to computational studies, recent in vitro studies using modern polymer-based microfluidic devices have attempted to mimic the flexibility of real vessels,[19] while still allowing for controlled manipulation of flow parameters. However, replicating the glycocalyx layer that coats the capillary endothelium remains a significant challenge.[20,21] Because this layer contributes to much of the cell-wall interaction in capillaries, its absence may undermine the physiological relevance of the observed cell partitioning behavior. Furthermore, in vitro partitioning models commonly adopt the Pries model's assumption that RBC volume is conserved across vascular bifurcations.[22,23] Although this assumption has been successfully applied at the arteriolar level, it may not be valid in capillaries. For instance, RBCs can rapidly release water into the surrounding fluid through aquaporin-1 channels when subjected to mechanical suction through narrow glass micropipettes.[24] Our recent retinal capillary flow imaging study also suggests that RBCs may release some of their intracellular fluid into the plasma within the narrowest capillaries, thereby reducing their size and friction during transit.[25] Therefore whether RBC volume is tightly conserved across capillary junctions requires further investigation through careful in vivo observations.

The current body of in vivo data on RBC partitioning at capillary junctions is limited, largely based on small-scale intravital microscopy studies in animals.[13,26–28] These studies require fluorescent dye injection and invasive tissue preparation, both of which may disrupt the natural state of capillary flow. Fortunately, advancements in adaptive optics (AO) imaging have made it possible to noninvasively visualize the human retinal capillary network and track single-cell blood flow,[29,30] enabling accurate measurement of velocity fluctuations across cardiac cycles,[31–34] RBC packing density in capillaries,[35,36] and cell shapes.[25,37]

We have recently used high-speed flood-illumination AO to report on the association of RBC size and shape with the diameter of the vascular lumen.[25,37] We observed that RBCs were smaller in smaller vessels, which we attributed in part to a filtration effect whereby larger cells "choose" wider branches, as well as to a loss of cell volume as cells squeeze through the narrowest vessels.[25] However, our prior analysis examined all trackable vessels independently, without considering their connectivity. In the present study, we targeted capillary junctions through which flow could be reliably observed both before and after the bifurcation to examine more directly how variations in lumen diameter affect the distribution and size changes of RBCs. By analyzing both diverging and converging junctions, we also explored whether the flow characteristics and distribution of RBCs on the arteriolar side of the capillary network differ from those on the venular side, an aspect often overlooked in previous analyses focused exclusively on diverging junctions. These findings provide empirical context that may enhance the physiological relevance of future in silico and in vitro models of capillary network flow.

Method

Subjects

Data were gathered from six healthy human adults aged 22 to 40 years (four females and two males) with no systemic or ocular health conditions. The study was approved by the University of Melbourne's Human Research Ethics Committee and conducted in compliance with the Declaration of Helsinki principles. The left eye of each participant was dilated with 1.0% tropicamide before the imaging session.

Imaging Location

Capillary junctions near the foveal avascular zone were targeted, where the single-layered capillary network arrangement enabled high-quality flow recordings without interference from deeper vessels. During image acquisitions, subjects fixated on an illuminated grid. Their fixation position was adjusted to bring the capillaries of interest into the 1.25° wide imaging field.

Adaptive Optics

Capillary flow was imaged using a flood-illumination AO ophthalmoscope, as described in previous publications.[3] In brief, an 835 nm reference beam from a superluminescent diode was directed onto the retina, and the returning light was sampled by a Shack-Hartmann wavefront sensor in a conjugate pupil plane. Ocular aberrations were corrected by a deformable mirror (ALPAO, Montbonnot-Saint-Martin, France) at 20 Hz, with defocus adjustments in increments of 0.05D until the capillaries at the intended depth appeared sharp. Image acquisition began once the root mean square of the wavefront aberration reduced to less than ~0.06 µm over a 7 mm pupil. For each acquisition, three seconds of flow data were recorded by a high-speed scientific CMOS camera (NEO, Andor Technology PLC, Belfast, UK) in global shutter mode at 200 to 400 fps. The 750 ± 25 nm imaging laser was passed through a 32 m multimodal optical fiber to reduce coherence and associated image speckle. Light power at the cornea was 0.3 mW to 1.3 mW, which maintained a safety factor of 10 times relative to the ANSI standards for maximum permissible exposure.[38]

Image Processing

Unless otherwise stated, all image processing was performed in MATLAB (R2022b; MathWorks, Natick, MA, USA) using custom-written scripts based on previously published algorithms.[25,34,37] Each recorded raw image sequence was background-subtracted, flat-fielded, and registered using two-dimensional (2D) cross-correlation to correct for eye movement during the image acquisition. The temporal variation in pixel intensity was used to produce motion contrast images, highlighting retinal blood flow against the stationary background tissue (Fig. 1A). RBC flow velocity was computed using pixel intensity cross-correlation (Fig. 1B).[34]

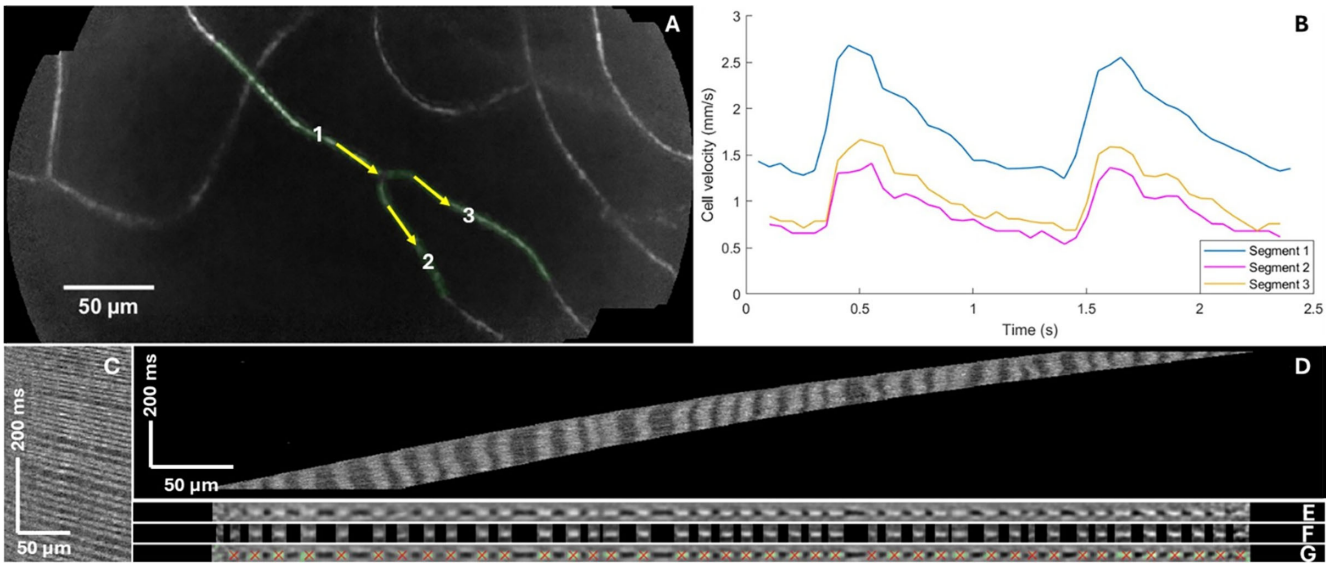

Figure 1. Image processing illustration. **(A)** Motion contrast image of a capillary area of interest, highlighting a diverging junction (*green*) where blood flows from segment 1 into segments 2 and 3. See Supplementary Video S1 for a one-second recording of blood flow through this junction, and Supplementary Video S2 for a recording of a converging junction. **(B)** RBC flow velocity profile for the three segments highlighted. **(C)** Spatiotemporal kymograph of segment 3, displaying intensity changes along the vessel centerline (horizontal axis) over time (vertical axis). Each bright band represents the change in RBC position over time, and dark bands represent plasma gap movement. Only 0.55 s of 3 s flow data is shown here for demonstration purposes. **(D)** Kymograph from **C** after motion correction. The same spatial scale applies to panels **E–G**. **(E)** Blood column image generated from all motion-corrected kymographs of streamlines parallel to the capillary centerline within the 12.5 µm wide sampled region. **(F)** RBCs segmented from plasma using principal components analysis to enable length-based hematocrit estimation; plasma gaps masked out for visualization. **(G)** RBC centroids marked by *red* "*x*." Distances between cell centroids were computed to quantify inter-cell distance.

From motion contrast images, the centerline of each capillary segment of interest was traced up to the junction point in Adobe Photoshop using a single-pixel pencil tool. Pixel intensities along these lines over time were used to create spatiotemporal kymographs (Fig. 1C). Because cells may appear either bright or dark depending on the plane of focus,[39] we reviewed the blood flow videos to determine the contrast polarity for each capillary segment. For consistency, segments in which RBCs appeared dark were contrast-reversed, so that bright bands in the kymographs always correspond to cells and dark bands to the plasma-filled gaps. To measure cell shapes, we extended the same process radially to produce a stack of kymographs for streamlines parallel to the flow centerline, spanning a radial distance of 12.5 µm.

Axial flow speed variations along the vessel, as demonstrated in our previous work on pulse wave propagation in retinal capillaries,[40] were not considered in this study. Instead, we applied the same velocity profile to correct for bulk motion displacement (Fig. 1D) in all kymographs for each capillary segment, assuming the diameter remains constant along its length. After this correction, each stack of kymographs was compressed along the time axis to generate a 2D blood column image in the axial and radial dimensions (Fig. 1E).

The application of the same velocity correction radially across the capillary lumen does not consider the varying flow velocities within the peripheral CFL. However, this does not affect the appearance of the blood column image, because the CFL was not visible in our recordings. Assuming a uniform speed for all parts of the cell also disregards real-time membrane motions, such as tank treading. Therefore the analysis presented in this study focuses on the time-averaged behaviors of the cells.

The method for measuring cell shape has been detailed in our previous work.[25,37] Because individual cell measurements are inherently limited by the instantaneous lateral resolution of our device (~2 µm for 750 nm imaging over an 8 mm pupil), we upscaled each blood column image by a factor of five to increase pixel density and enable more robust averaging of cell shape at the segment level. From the upscaled images, RBCs were segmented from plasma based on their distinct intensity profiles, allowing hematocrit to be estimated as the fraction of the blood column length occupied by cells (Fig. 1F). This segmentation also enabled identification of each cell's centroid and calculation of the spacing between neighboring cells (Fig. 1G). Based on the centroid locations, individual cells were extracted from the thresholded blood column image and overlaid to create a probability map (Fig. 2B), describing the likelihood of a pixel being classified as "cell" relative to its distance from the cell centroid. Pixels with a probability value greater than 50% were considered part of the cell (Fig. 2C), and the outline of these pixels was smoothed to better define the cell shape (Fig. 2D).

We note that inaccuracies in individual RBC centroid marking can introduce misalignment blur in the averaged intensity profile. In this regard, thresholding the probability helps mitigate the effects of extreme centroid marking errors. For example, when hundreds of binarized cells within each vessel are aligned by their centroids and superimposed, cells with poorly located centroids mainly contribute to peripheral pixels with low probability scores, making them unlikely to meet the >50% threshold used to define the average cell boundary. Minor misalignments, however, may still result in residual sub-micron blur that is not fully eliminated by this process.

Investigative Ophthalmology & Visual Science

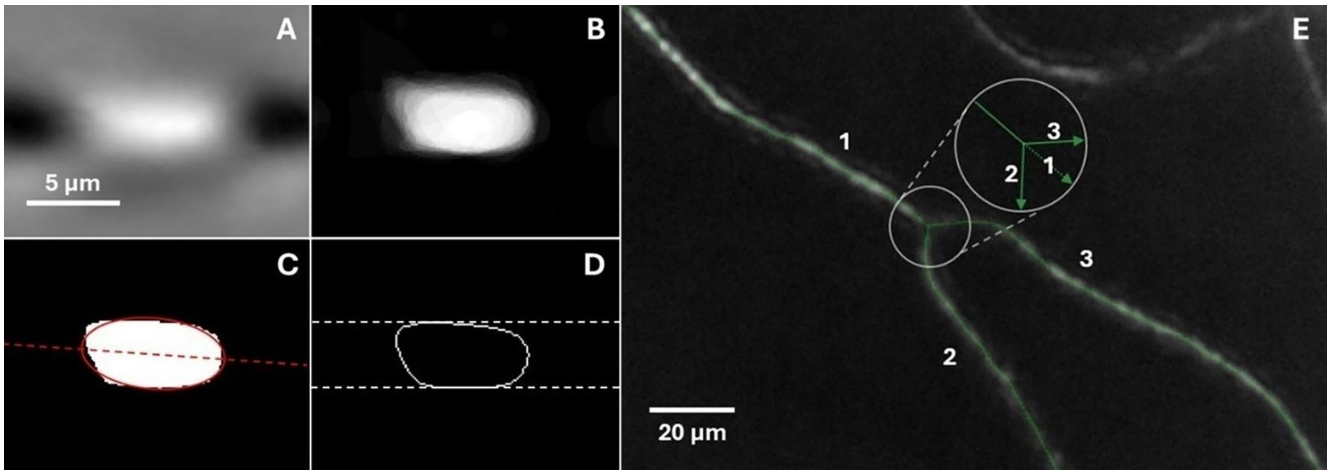

Figure 2. 2D analysis of average cell shapes and branching angles. **(A)** Average axial-radial intensity profile of RBCs in segment 3, corresponding to the same segment 3 highlighted in Figure 1. The same scale applies to panels **B–D**. **(B)** Probability map of the average cell, where pixel intensity represents the likelihood of each pixel being part of a cell. **(C)** Ellipse (*red*) fitted to the cluster of pixels with probability values greater than 50%. The long axis of the ellipse defines the inclination angle of the cell relative to the flow axis. **(D)** Smoothed cell border derived from the binarized average cell shown in **C**, where the upper and lower edges define the channel boundary (*white dashed line*) within which the cells flow. **(E)** Bifurcation region defined with a radius equal to twice the largest channel size determined in **D** for the three vessels. The branching angle is calculated using vectors: the vector for the main vessel is oriented toward the junction point, whereas vectors for the branch vessels are oriented away from it.

The binarized probability image of the average cell was fitted with an ellipse, and the angle between its longest axis and the direction of flow determines the cell's orientation (Fig. 2C). The upper and lower bounds of the smoothed cell contour define the channel size through which cells travel (Fig. 2D). As in our previous work,[25,37] we refer to the diameter of this functional cell passage channel as "lumen diameter," although it does not account for the CFL thickness, which was not readily visible in our images.

Using lumen diameter data, we defined a circular bifurcation region centered at the junction point, with a radius set to twice the largest diameter among the three capillary branches (Fig. 2E). Within this region, a linear best-fit was computed for each of the three manually traced vessel centerlines. Following established practices,[41] deviation angles were estimated by deriving vectors from the best-fit lines, with the origin set at the junction point. The deviation angle for each branch vessel was calculated using the inverse cosine of the dot product between its vector and the main vessel vector, normalized by the product of their magnitudes. The resulting angles fell within the range of 0° to 180°.

To estimate cell size, we applied our previously developed method that uses the 2D cell profile together with the assumption of a circular lumen to spin out a pseudo-3D shape.[25] In Figure 2D, each image column of the cell contour was rotated around the midline between the two pixels defining the upper and lower cell border. This generated a 3D point cloud that delineated the 3D outline of the average cell (Fig. 3A). The *alphaShape()* function in MATLAB was used to bound the cell surface (Fig. 3B) and estimate its surface area and volume. For simplicity, we refer to this technique as the "solid of revolution" method.

Estimation of Cellular and Total Blood Flow Rates

Assuming a circular vessel lumen with a constant diameter along its length, the volumetric flow rate for total blood (Q_b) and RBCs (Q_r) can be empirically calculated from the mean flow velocity (v), the lumen diameter (D) and hematocrit (H):

$$Q_b = v\left(\frac{D}{2}\right)^2 \pi \tag{1}$$

$$Q_r = Q_b\, H \tag{2}$$

The fractional flow (FQ) in one branch vessel is defined as the ratio of the flow in that branch to the total flow in both branch vessels, applicable to both total blood (FQ_b) and RBCs (FQ_r):

$$FQ_1 = \frac{Q_1}{Q_1 + Q_2} \tag{3}$$

The Pries Model

The Pries model[10–12] predicts the fractional RBC flow (FQ_r) in the branch vessel of an arteriolar junction based on the fraction of blood flow it receives (FQ_b), the diameter of all three vessels in the junction (D_f, D_1 and D_2), and the hematocrit in the feeding vessel (H_f):

$$logit\left(FQ_r\right) = A + B\, logit\left(\frac{FQ_b - X_0}{1 - 2X_0}\right) \tag{4}$$

where

$$logit\left(p\right) = log\left(\frac{p}{1-p}\right) \tag{5}$$

$$A = -13.29\,\frac{(D_1^2/D_2^2) - 1}{(D_1^2/D_2^2) + 1}\left(\frac{1 - H_f}{D_f}\right) \tag{6}$$

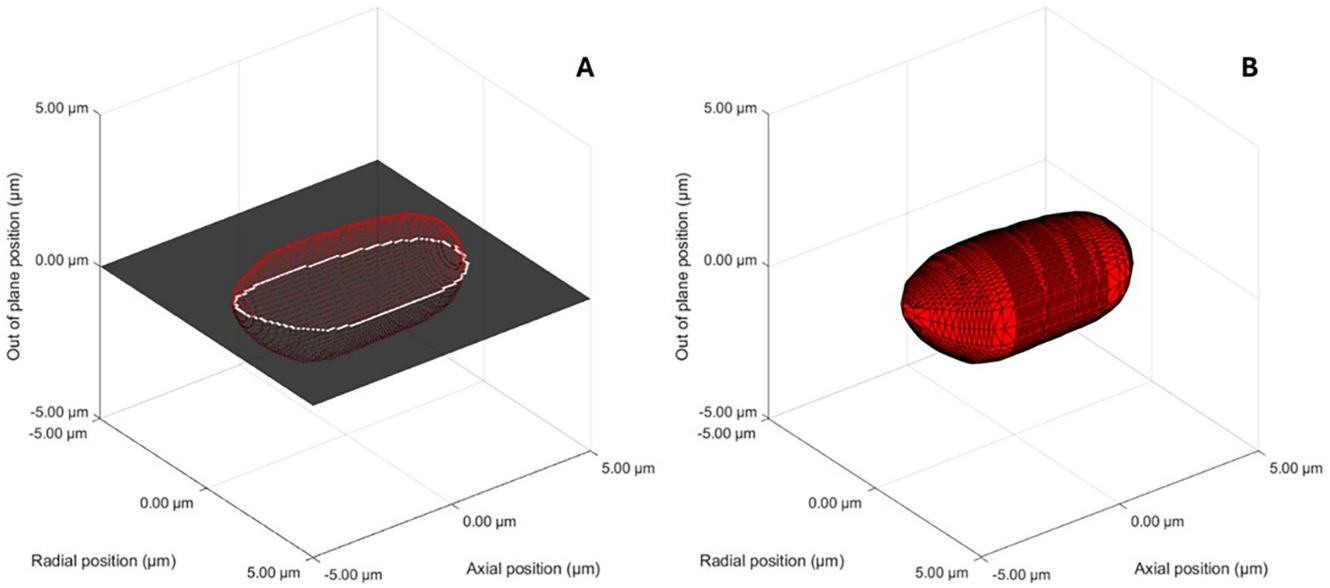

Figure 3. Reconstruction of pseudo-3D cell shapes. **(A)** A 3D point cloud representation of a cell, inferred from its 2D contour. **(B)** Cell surface reconstructed from the point cloud in **A**.

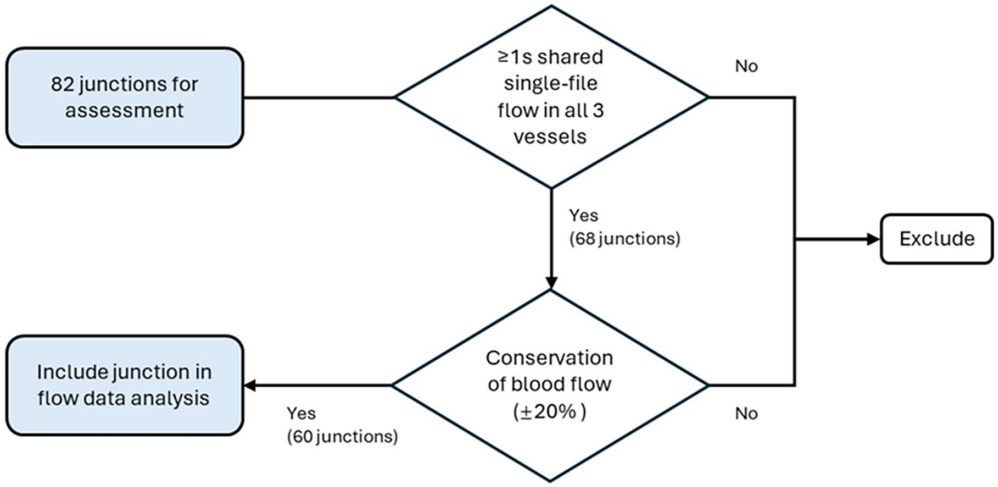

Figure 4. Process for selecting junctions included in flow analysis. Junctions were excluded if they did not have at least one second of clear single-file flow in all three vessels or if they failed the blood flow conservation (i.e., Q_b main vessel = Q_b branch 1 + Q_b branch 2) criterion within ±20%.

$$B = 1 + 6.98\left(\frac{1 - H_f}{D_f}\right) \tag{7}$$

$$X_0 = 0.964\left(\frac{1 - H_f}{D_f}\right) \tag{8}$$

For a given feeding vessel diameter (D_f) and feeding hematocrit (H_f), X_0 represents the threshold of fractional blood flow (FQ_b) below which a downstream branch receives only plasma and no RBCs ($FQ_r = 0$). Accordingly, the other branch ($FQ_b > 1 - X_0$) takes all the cells from the inflow vessel ($FQ_r = 1$).

As the present study includes diverging and converging junctions, we extend the Pries model to accommodate both by defining the feeding vessel as the "main vessel" in diverging junctions and the collecting vessel as the "main vessel" in converging junctions, with the remaining two classified as "branch vessels."

Capillary Junction Selection Criteria

Junctions were screened for inclusion in flow data analysis using a two-step selection process (Fig. 4). Although imaging was performed near the fovea, where the capillary network has a single stratification, its geometric arrangement is unlikely to be completely planar. Junctions with high-quality blood column images that failed the blood flow conservation criterion (±20%) were likely affected by unreli-

Investigative Ophthalmology & Visual Science

able diameter or velocity measurements because of capillaries being angled out of the imaging plane and were excluded on this basis.

Results

Comparison Between Diverging and Converging Junctions

Among the six subjects imaged, 60 junctions across 26 retinal regions met the selection criteria and were included in the cell partitioning analysis. On average, each junction provided 2.4 ± 0.7 seconds (mean ± SD) of continuous flow data. The mean traced capillary length was 54 ± 30.5 µm, with 193 ± 119 cells observed per capillary segment during the recording period, yielding a total of 34,804 RBC appearances included in the flow distribution and cell size analysis.

Basic flow parameters, such as cell velocity, lumen diameter, hematocrit, cell surface area, cell volume, linear cell density, inter-cell distance, and cell inclination angle to the flow axis, were measured across the 180 capillary segments corresponding to these junctions (Table 1). No significant differences were observed in the mean of each parameter between diverging and converging junctions, indicative of comparable flow environments within each.

Beyond comparing mean outcome measures, we also assessed the asymmetry between branches at each junction. We defined a branching angle asymmetry factor as the ratio of the larger to the smaller deviation angle of the two branch vessels from the main vessel, and blood flow and RBC flow asymmetry factors as the ratio of flow in the higher-flow branch to that in the lower-flow branch. These metrics of asymmetry again showed no significant differences between diverging and converging junctions, allowing the data to be pooled for subsequent analysis.

In addition, we explored whether cell lingering might be reflected in differences in the variability of inter-cell spacing between the two junction types. The distributions of inter-cell spacing standard deviations did not differ significantly (see Supplementary Figure S3).

Performance of the Pries Model to Predict Cell Partitioning

With pooled data from 60 capillary junctions, we assessed the predictive accuracy of the Pries model at the capillary level. Although a strong correlation ($R^2 = 0.73$) was observed between the predicted and experimental fractional RBC flow (FQ_r) values, Figure 5A shows that the Pries model tended to under-predict FQ_r at low fraction of blood flow (FQ_b) and over-predict it at high FQ_b values. To improve the model's fit, we used the *fmincon()* function in MATLAB to optimize the empirically determined coefficients in the Pries model by minimizing the root mean square error. This optimization improved the R^2 value to 0.78 (Fig. 5B), suggesting the Pries model's logistic regression framework remains applicable, even though the original model was calibrated for a different tissue and species, and applied to slightly larger vessels located only on the arterial side of the circulation.

Because our observations did not include extreme cases where one branch received all cells and the other carried only plasma, it was not possible to empirically determine the fractional blood flow threshold (X_0) defined by Pries, below which a branch is assumed to carry plasma only. Therefore we removed X_0 along with its constituent variables, H_f and D_f (where H_f denotes the hematocrit in the main vessel and D_f is its diameter) from the Pries model, and re-optimized the coefficients to minimize the fitting error. This simplified model achieved a R^2 value of 0.80, comparable to the optimized Pries model with all variables included (Figs. 5B, 5C), suggesting that X_0, H_f and D_f do not significantly affect the distribution of RBC flow in capillary branches. The simplified Pries model fit to our data is described by:

$$logit\left(FQ_r\right) = 0.088 * \frac{\left(D_1^2/D_2^2\right) - 1}{\left(D_1^2/D_2^2\right) + 1} + 1.47 * logit\left(FQ_b\right) \quad (9)$$

Using this simplified model, the RBC flow distribution (FQ_r) at capillary junctions can be predicted based on the fractional blood flow distribution (FQ_b) and the diameters of the two branch vessels (D_1, D_2). Recognizing that junction geometry involves more complexity than branch vessel size alone, we further assessed the effects of branching angle on cell distribution.

Predicting RBC Distribution From Junction Geometry

Consistent with earlier findings from in vitro[42,43] and in vivo[10] RBC partitioning studies, as well as predictions from 2D microvascular flow simulations,[44] we observed no significant effect of deviation angle from the main vessel on cell distribution in branch vessels (Figs. 6A, 6B). This aligns with the classic view in microvascular flow dynamics that RBC

Table 1. Basic Flow Parameters for 32 Diverging and 28 Converging Capillary Junctions

	Diverging Junction		Converging Junction		Comparison		
Parameters	**Mean ± SD**	**95% Range**	**Mean ± SD**	**95% Range**	**Δ Sample Mean**	**95% CI**	***P* Value**
Cell velocity (mm/s)	1.48 ± 0.59	0.59 to 2.71	1.37 ± 0.49	0.47 to 2.60	0.11	−0.05 to 0.28	0.32
Lumen diameter (µm)	4.60 ± 0.75	3.38 to 6.36	4.58 ± 0.71	3.36 to 6.14	0.03	−0.18 to 0.25	0.99
Hematocrit (%)	45.8 ± 11.1	21.0 to 65.0	48.4 ± 11.8	25.2 to 70.1	−2.60	−6.00 to 0.75	0.13
Cell surface area (µm^2)	92.06 ± 22.15	53.6 to 138.2	90.42 ± 22.8	51.9 to 130.2	1.64	−4.99 to 8.25	0.63
Cell volume (fL)	74.97 ± 25.28	36.3 to 137.0	72.95 ± 25.43	34.5 to 121.4	2.02	−5.45 to 9.50	0.64
Linear cell density (cells/mm)	55.91 ± 19.29	22.63 to 93.99	57.49 ± 18.25	28.13 to 91.03	−1.58	−7.12 to 3.97	0.58
Inter-cell distance (µm)	20.54 ± 8.64	10.60 to 44.40	19.54 ± 6.86	11.0 to 35.3	1.00	−1.32 to 3.32	0.59
Cell orientation (°)	−0.24 ± 27.9	−75.7 to 76.7	0.47 ± 22.6	−48.6 to 54.8	−0.71	−8.26 to 6.82	0.85
Branching angle asymmetry factor	2.58 ± 3.30	1.01 to 15.63	3.22 ± 3.31	1.10 to 14.29	−0.64	−2.17 to 1.03	0.51
Blood flow distribution asymmetry factor	2.13 ± 1.13	1.06 to 5.55	1.82 ± 0.77	1.01 to 3.83	0.31	−0.20 to 0.82	0.23
RBC flow distribution asymmetry factor	3.53 ± 3.18	1.19 to 14.29	2.69 ± 1.85	1.12 to 7.21	0.84	−0.53 to 2.21	0.22

Differences in sample means were calculated as the metric for diverging junctions minus that for converging junctions, with 95% confidence intervals and *P* values derived from 100,000 bootstrap iterations.

Investigative Ophthalmology & Visual Science

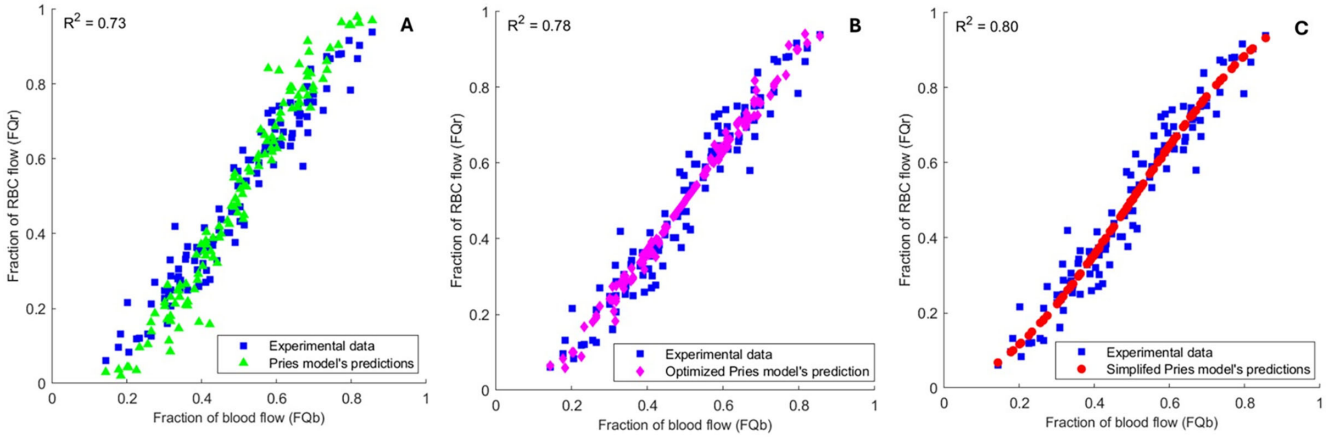

Figure 5. Optimization and simplification of the Pries model for predicting RBC flow distribution. **(A)** Pries model predictions versus empirical measurements, showing a general trend of under-prediction of FQ_r at low FQ_b values and over-prediction at high FQ_b values. **(B)** Pries model with optimized coefficients to improve fit to our observations. **(C)** Simplified Pries model fitted to our observations, showing an R^2 of 0.80, comparable to the optimized Pries model in **B** with all variables included. Because both FQ_r and FQ_b are fraction metrics, the value from one branch inherently predicts that of the other within the same junction. Therefore only data from the 60 higher-RBC-flow branches were used for R^2 calculations in **A–C** to prevent artificially inflating R^2 values.

movement in capillaries is primarily governed by viscous forces, with the inertia of flowing RBCs being negligible,[7] such that a smaller deviation angle from the main vessel does not guarantee a preference for cell entry into one branch over the other.

In contrast, the cross-sectional area of the branch vessel had a significant impact (Figs. 6C, 6D), with a linear model explaining 21% of the variance in hematocrit ($H = 0.62 \times$ fraction of cross-sectional area $+ 0.14$; $P < 10^{-6}$) and 25% of the variance in RBC flow distribution ($FQ_r = 0.76 \times$ fraction of cross-sectional area $+ 0.28$; $P < 10^{-4}$). The reduced concentration of RBCs in the branch vessel with a smaller lumen (Fig. 6C) suggests that cell deformation, although important, does not necessarily allow free passage through the narrowest capillaries. The difficulty in entering narrow branches aligns with our previous observation of a network filtration effect, where cells appear smaller and more spaced out in narrower vessels.[25] A similar trend between capillary diameter and cell size was observed in the 60 non-connected main vessels of the present dataset, with capillary diameter positively correlating with both cell surface area ($r = 0.59$; $P < 10^{-6}$) and cell volume ($r = 0.67$; $P < 10^{-8}$). However, on paired branch analysis at the junction level, no significant difference in cell size was observed between the wider and narrower branch. This is likely because branch diameter variation within junctions was too small to reveal a filtration effect.

A Single-Variate Linear Partitioning Model

We have demonstrated that removing parameters related to the main vessel (hematocrit H_f; diameter D_f) and the threshold term (X_0) from the Pries model had minimal impact on its predictive accuracy ($R^2 = 0.80$ for the simplified model versus $R^2 = 0.78$ for the full model with updated coefficients). In contrast, excluding the flow information and relying solely on junction geometry significantly reduced predictive accuracy ($R^2 = 0.25$; Fig. 6D). Next, we investigate whether hematocrit (H) and red cell flow distribution (FQ_r) in branch vessels can be predicted from fractional blood flow (FQ_b) alone, without explicit reference to junction geometry parameters (i.e., D_1, D_2), thus further simplifying the model.

A moderate positive correlation was found between FQ_b and hematocrit in the branch vessel ($H = 0.43 \times FQ_b + 0.24$; $R^2 = 0.32$, $P < 10^{-10}$), showing that RBCs were more prevalent in the branch vessel with a higher volumetric flow rate. This aligns with predictions from numerical microvascular flow simulations[18,45] that faster flow rate corresponds to lower downstream resistance, making it easier for cells to enter.

The scatter of the observed FQ_b and FQ_r values significantly deviated from the "$FQ_r = FQ_b$" line (Fig. 7B). This line represents the expected cell partitioning behavior at macrovascular junctions, where RBCs distribute uniformly in the blood, comparable to a solute in a homogeneous solution. In such a scenario, the RBC concentrations across two branch vessels would be equal, regardless of their flow rates. Here, most FQ_r values exceeded FQ_b values when $FQ_b > 0.5$ and were lower than FQ_b values when $FQ_b < 0.5$, indicating a clear bias in RBC distribution that favors the branch with higher blood flow, as also reflected in the positive correlation observed between hematocrit and FQ_b (Fig. 7A). The fraction of RBC flow in branch vessels can be predicted from the fraction of blood they receive using a linear relationship ($R^2 = 0.79$; $P < 10^{-20}$):

$$FQ_r = 1.34 * FQ_b - 0.17 \quad (10)$$

The slope of the linear model being greater than 1.0 indicates high resistance to RBC flow in the capillaries examined in this study, where changes in total blood flow have a disproportionately large impact on RBC entry and passage. This finding aligns with our earlier observation that in capillaries with diameters within or below the range of 4.1 to 5.3 µm, even small reductions in lumen diameter can significantly affect RBC density and packing.[25] Building on this, extrapolating the linear model slightly beyond our empirically measured FQ_b (0.14–0.86) and FQ_r (0.06–0.94) ranges suggests that a branch vessel with a fractional blood flow below 12.7% could carry only plasma without RBCs.

Investigative Ophthalmology & Visual Science

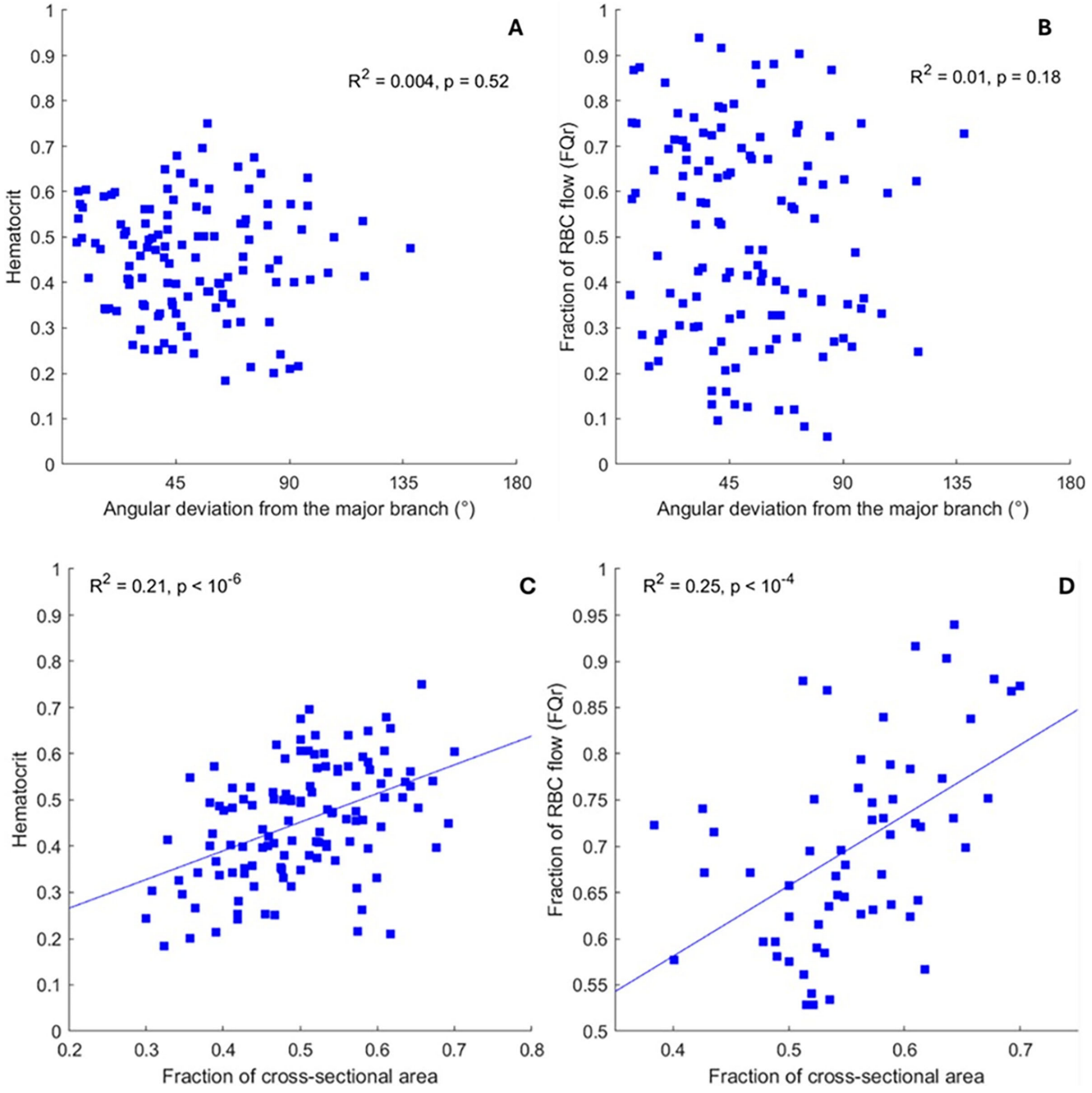

Figure 6. Relationship between junction geometry and RBC distribution in the branch vessel. The angular deviation from the main vessel showed no significant correlation with **(A)** hematocrit and **(B)** the fraction of RBC flow in the branch vessel. Conversely, the fraction of cross-sectional area, calculated as the squared lumen diameter for one branch divided by the sum of the squared lumen diameters of both branch vessels, showed a significant moderate positive correlation with **(C)** hematocrit and **(D)** the fraction of RBC flow in the branch vessel. Only data from the 60 higher-RBC-flow branches were plotted in **D** and used for R^2 calculation because of the complementary nature of fraction metrics.

Comparison of Model Prediction Accuracy

We compared the prediction performance of four RBC partitioning models described earlier, with root mean square error values presented in Figure 8. A one-way ANOVA of the squared fitting errors for the optimized Pries model, simplified Pries model, and linear model revealed no significant differences in fitting quality ($P = 0.90$). In contrast, the original Pries model had a significantly higher squared fitting error than the other three models indicating its reduced accuracy at the capillary junctions in the human retina (pairwise *t*-tests with Bonferroni correction: $P = 0.006$ vs. the optimized Pries model; $P = 0.002$ vs. the simplified Pries model; $P = 0.004$ vs. the linear model).

Change in Cell Size Across Junctions

The main vessel of each capillary junction had a significantly larger lumen diameter (4.93 ± 0.75 µm, mean ± SD) than the two branch vessels (4.43 ± 0.66 µm, mean ± SD;

Investigative Ophthalmology & Visual Science

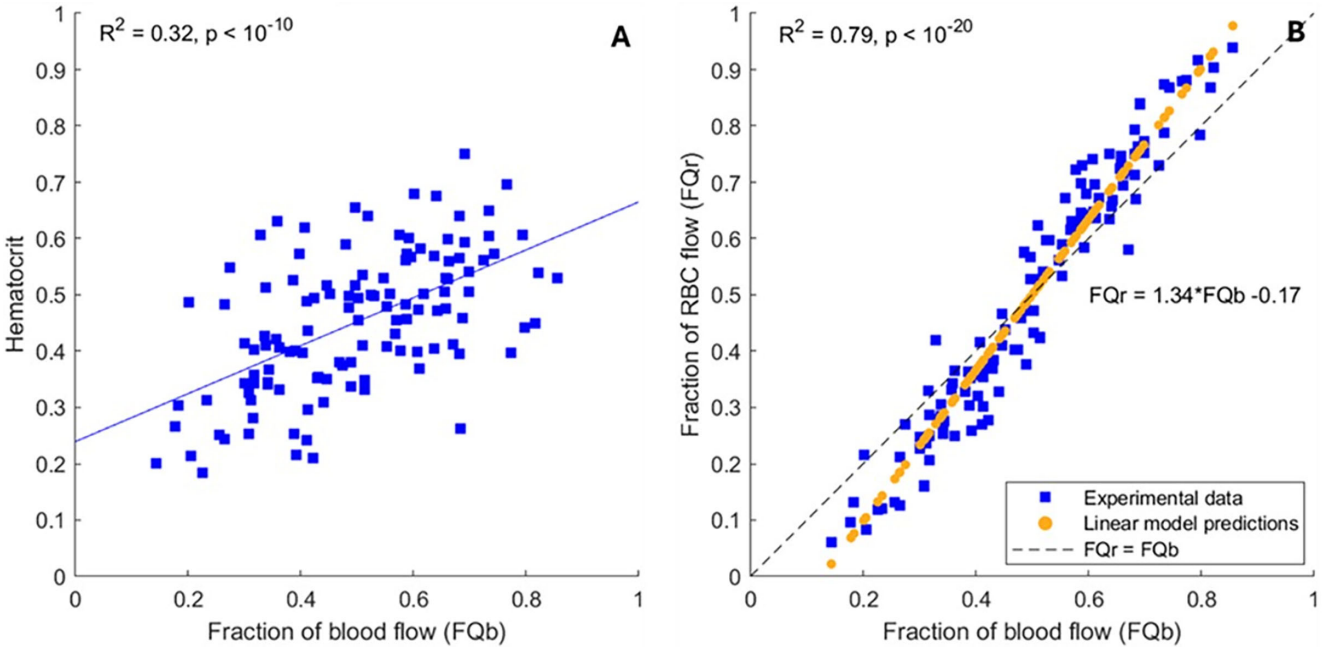

Figure 7. Relationship between blood flow distribution and RBC distribution. **(A)** Branch vessel with a higher blood flow generally had a higher hematocrit. **(B)** A strong positive correlation between FQ_b and FQ_r. The *dashed line* represents the "$FQ_b = FQ_r$" scenario, where both branch vessels receive the same hematocrit regardless of their fraction of blood flow. A univariate linear model predicted FQ_r based on FQ_b. The R^2 value in **B** was calculated from 60 higher-RBC-flow branches only.

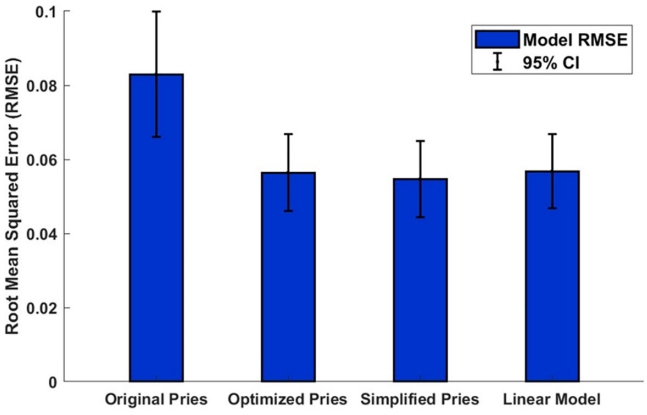

Figure 8. Comparison of model predictions and fit quality. Root mean squared fitting error for each model, with 95% CI obtained by bootstrapping prediction errors 100,000 times. Only data from the 60 branches with higher RBC flow were used for bootstrapping and RMSE calculations.

$P < 10^{-5}$). This vessel size disparity suggests that RBCs face increased radial constraints within the branches, potentially leading to cell size changes as they adapt to the narrower lumen. To investigate this, we examined changes in cell size, hematocrit, and cell spacing across each of the 60 junctions included in the cell partitioning analysis (Table 2).

To enable a paired comparison between the main vessel and the two branch vessels at each junction, for each metric listed in Table 2, we calculated an average for the two branches, weighted based on their RBC volumetric flow rate. A paired-sample *t*-test between the major vessel and the branch average showed that cells in the branch vessels had a similar surface area to those in the main vessels, as expected, given the limited ability of RBCs to stretch their membrane without rupture.[46] In contrast, cell volume in the branch vessels was on average 4.20 fL (or 5.5%) lower than in the main vessels ($P = 0.029$). To provide an additional perspective on this finding, we re-estimated cell volume change under the assumption that cell surface area stays constant between the main vessel and its two branches at each junction. Applying the empirical power law relationship between surface area and volume ($SA \propto V^{2/3}$),[47] this alternative approach yields a reduction of 3.07 fL (or 4.0%) of cell volume in branch vessels, with stronger statistical significance ($P < 10^{-4}$). Alongside the decrease in cell volume, branch vessels were found to have a 3.0% lower hematocrit ($P < 10^{-4}$) and a 2.3 µm increase in inter-cell spacing ($P < 10^{-4}$), suggesting a dynamic exchange of incompressible fluid between cells and plasma as capillary size changes, as discussed further below.

Discussion

Using flood illumination AO imaging and established image processing methods, we measured RBC flow distribution and cell size changes across 60 capillary junctions in the human retina. In this sample, the fraction of RBC flow in capillary branches could be reasonably predicted without relying on the main vessel flow information required by the Pries model. Notably, none of the logistic regression-based cell partitioning models outperformed a simple linear predictor based solely on the flow rate of whole blood. Junction-level analysis revealed that plasma gaps between cells were consistently longer in branch vessels than in the main vessel. Taken together with the concurrent reductions in average cell volume and hematocrit, these findings support the possibility of fluid movement from RBCs to plasma in capillary

Investigative Ophthalmology & Visual Science

Table 2. Changes in Cell Size, Hematocrit, and Cell Spacing From the Main Vessel to Branch Vessels

Parameters	Main Vessel (Mean)	Branch Vessel Pair (Mean)	Comparison Using Paired Samples *t* Test		
			Mean Difference ± SEM	95% CI	*P* Values
Cell length (μm)	8.58	8.63	−0.05 ± 0.24	−0.53 to 0.43	0.84
Cell surface area (μm^2)	91.30	90.63	0.66 ± 1.66	−2.65 to 3.98	0.69
Cell volume (fL)	76.99	72.79	4.20 ± 1.87	0.46 to 7.94	0.029
Hematocrit (%)	50.51	47.49	3.02 ± 0.63	1.76 to 4.27	$<10^{-4}$
Inter-cell distance (μm)	17.43	19.74	−2.31 ± 0.49	−3.29 to −1.32	$<10^{-4}$

Parameters for each pair of branch vessels were calculated as weighted sums based on their RBC flow rates. The mean difference represents the average of differences in paired observations from each junction (i.e., main vessel - branch vessels). The 95% CI and *P* values were obtained from a paired samples *t*-test.

branches, and reabsorption into RBCs upon entry into a collecting vessel.

No Significant Difference Between Junction Types

The basic flow parameters and asymmetries in flow distribution and branching geometry, all of which are likely to influence cell partitioning, did not differ significantly between diverging and converging junctions. This may be partly due to only junctions with single-file flow being included in the analysis. In microvascular junctions with multi-file flow, converging junctions can be easily distinguished in split-detector adaptive optics scanning light ophthalmoscopy images, where the cell-free regions from two branches extend into the collecting vessel as streamlines that demarcate the inflows.[48] In our current dataset of single-file flow junctions, we believe the blood flow is sufficiently non-turbulent to be, in principle, reversible, and there are no apparent visual cues to distinguish the actual flow direction if the image sequence were played in reverse. Therefore, pooling data from both junction types is a pragmatic simplification.

We also explored whether cell lingering could be inferred from differences in inter-cell spacing variability between the two junction types. As lingering involves a momentary pause of RBCs near the bifurcation apex of diverging junctions, its transient and stochastic nature would be expected to increase cell spacing variability. Accordingly, if lingering were a major contributor to the time-averaged RBC partitioning behavior, we would expect greater dispersion of inter-cell distances in segments from diverging junctions. However, no significant difference in the standard deviation of inter-cell spacing was found between two junction groups (Supplementary Figure S3), suggesting that lingering may not play a major role. This inference remains preliminary, as the resolution within the bifurcation region is insufficient to directly observe or rule out cell lingering events.

Cell Volume Change Across Capillary Junctions

At vascular junctions, knowing the flow rate in any two vessels allows for prediction of the third, based on the conservation of volume. This creates an inherent redundancy in the raw data collected from all three vessel segments. In light of this, Pries et al.[10] proposed that the volumetric flow rate and hematocrit measurements in the three vessels should be scaled based on the magnitude of flow rates, ensuring consistency with the conservation of total blood flow (Q_b main = Q_b branch 1 + Q_b branch 2) and RBC flow (Q_r main = Q_r branch 1 + Q_r branch 2). This method assumes measurement errors to be proportional to the measured flow values, with vessels of higher flow having larger measurement errors. The approach has since been adopted by several studies investigating RBC distribution at capillary bifurcations,[13,22,23] aiming to reduce the experimental noise in measured blood flow and hematocrit values.

Although this scaling method is appropriate for arterioles, where cell size is generally small compared to the vessel lumen, the fact that most capillaries are narrower than the undeformed size of an RBC raises uncertainty about whether cell volume stays constant as the lumen size changes across a junction. For example, RBCs can lose up to 12% of their volume when sucked through a micropipette, which they readily reabsorb on release.[46] RBCs in narrower retinal capillaries are also found to have lower volumes than those in wider capillaries, with most capillary diameters barely exceeding the theoretical minimum needed for cell passage.[25] These findings suggest that RBCs may experience volume loss in narrow capillaries. Given this consideration, scaling adjustments proposed by Pries[10] were not applied to our raw data.

In our previous work where capillary segments were considered independently of their connectivity, we estimated that each 1 μm decrease in lumen diameter would correspond to a 4.6 fL reduction in cell volume, assuming a constant cell surface area.[25] Given that the main vessels in the current study were, on average, 0.5 μm wider than the branch vessels, an average reduction of 2.3 fL (or 3.0%) in cell volume would be expected in branch vessels. This is lower than the 4.2 fL (or 5.5%; $P < 0.05$) volume reduction derived from our raw empirical cell size estimates, but closer to the 3.07 fL (or 4.0%; $P < 10^{-4}$) reduction calculated based on the assumption of no change in cell surface area across the junction. In light of the typical 11% to 15% distribution width of RBC volume in circulation,[49] the 5.5% change reported here may appear small. However, it is important to note that the former reflects the overall spread of sizes across the entire circulating RBC population, whereas the latter represents a subtle shift in the population mean across the bifurcation point. Given that some degree of network-level filtration likely occurs at the capillary level,[25] whereby larger cells may bypass narrower junctions via alternative paths, the average change in cell volume from main to branch vessels is not expected to match the full distribution width observed in ex vivo venous blood samples.

Given the ∼2 μm lateral resolution of our device, the estimated 4.2 fL change in cell volume cannot be resolved at the single-cell level. With 34,804 RBC appearances included in the cell size analysis and 193 ± 119 cells (mean ± SD) averaged per capillary segment, the signal-to-noise ratio is expected to substantially improve at the segment-averaged

Investigative Ophthalmology & Visual Science

cell level. To evaluate whether such small changes in mean cell volume between paired vessel groups can be reliably detected under our imaging constraints, we applied our processing pipeline to synthetic RBC images qualitatively resembling the experimental data (Supplementary Material S4). Despite the small effect size and measurement noise at the level of individual vessel pairs, femtoliter-scale changes in average cell volume were consistently detectable at the group level using a paired *t*-test, given our current sample size and number of paired observations.

Furthermore, if the 4.2 fL cell volume loss were solely an artefact of image processing, a corresponding reduction in surface area would be expected, since both metrics are derived from the same pseudo-3D model. The absence of a significant change in cell surface area (Table 2) is therefore reassuring. Complementing this, the increase in inter-cell spacing in branch vessels (2.3 ± 0.49 µm; mean ± SEM; $P < 10^{-4}$) lies within the system's lateral resolution limits and does not rely on assumptions in our pseudo-3D model. In the absence of a significant cell length change (Table 2), the increased spacing between cell centroids suggests longer plasma gaps between cells in branch vessels. In this context, the 3.0 ± 0.63% drop in hematocrit (mean ± SEM, $P < 10^{-4}$) and 5.5% reduction in average cell volume both point to RBCs as a potential source of this increased fraction of plasma volume. This is consistent with the hypothesis that water may be expelled from RBCs into the plasma as cells undergo radial compression in capillary branches.

The physiological significance of cell volume loss in capillary branches remains uncertain. On one hand, as RBCs lose water, the denser packing of hemoglobin molecules is expected to steepen the oxygen diffusion gradient, thereby enhancing oxygen offloading. Additionally, a reduction in lumen diameter in capillary branches reflects a shorter diffusion path to the vessel wall, which further facilitates gas exchange.[50] However, these benefits could be offset by other mechanisms. For instance, an increased hemoglobin concentration could result in a more tortuous intracellular diffusion pathway, hindering oxygen movement across the cytoplasm.[51] Furthermore, gas conductance through the cell membrane is thought to increase with osmotic swelling,[51] raising the possibility that cell shrinkage in branch vessels may reduce membrane permeability to gases. Given the inconclusive evidence, we speculate that the dynamic volume exchange between RBCs and plasma may help modulate gas exchange to benefit tissue health, although it is unclear whether this modulation promotes increased or decreased oxygen offloading in narrow capillary branches.

Although the short distance across a capillary junction may seem to limit the potential for significant RBC volume adjustments, the presence of aquaporin-1 channels on the RBC membrane[52] enables rapid water transport, making such changes physiologically feasible. In response to changes in osmolarity, RBCs can shrink up to 40% after losing all free water in the cytoplasm[53] or swell by 74% before lysis.[54] In synthetic capillary channels, such water exchange with the surrounding fluid completes within 60 ms in healthy RBCs with normal aquaporin-1 expression,[53] whereas genetically modified RBCs lacking aquaporin-1 show much slower kinetics and minimal volume change. In the current study of capillary flow in healthy individuals, the average path length from the start of a main vessel to the end of a branch vessel is approximately 108 µm. Assuming an average RBC flow speed of 1.5 mm/s, this path length allows ample time (i.e., ~72 ms) for the observed percentage of cell volume change to occur.

Deviation From the Pries Model's Predictions

The observed RBC flow distribution at human retinal capillary junctions deviates from the predictions of the Pries model,[10–12] as evidenced by the need to update its coefficients for better fit and the significantly higher root mean square error compared to models calibrated to our data. The deviation likely results from a combination of differences in vessel size, tissue type, species-related RBC rheology and experimental methods, as explored further below.

First, the Pries model was developed using data from arterioles with diameters of approximately 10–30 µm. Within this diameter range, the CFL surrounding the flowing RBCs is estimated to be 1.2–1.7 µm thick and is believed to play an important role in governing RBC partitioning at arteriolar junctions.[10] Specifically, the narrower branch tends to receive a higher fraction of plasma, commonly referred to as "plasma skimming,"[55] whereas most RBCs are directed toward the wider branch, which typically carries a higher blood flow. This plasma skimming effect underpins the sigmoidal relationship between fractional RBC flow (FQ_r) and fractional blood flow (FQ_b) described by Pries et al.[10–12] where branches receiving more than 50% of the blood flow attract a disproportionately larger share of RBCs, whereas those receiving less than 50% gain a smaller fraction of RBC flow than expected.

By comparison, the capillaries in the present study averaged 4.6 µm in diameter. In such narrow vessels, given the significant deformation required of RBCs for passage, the presence of a substantial CFL is unlikely.[13] This expectation is supported by early intravital observations of hamster cremaster muscle capillaries,[14] where fluorescent dye labeling of the free-flowing plasma revealed an average functional lumen diameter of 4.3 ± 0.2 µm (mean ± SE), comparable to the 4.6 µm in our sample. In these hamster vessels, RBC width averaged 3.9 ± 0.2 µm (mean ± SE), suggesting an annulus of free-flowing plasma approximately 0.2 µm thick around the RBCs. Such a thin layer is beyond the resolution of our imaging device. With the significant thinning of CFL, the effect of plasma skimming is expected to be less significant. This is consistent with our observation of a less sigmoidal trend in the FQ_r versus FQ_b scatter compared to the predictions of the Pries model (Fig. 4A).

Furthermore, whereas RBCs in arterioles and venules typically concentrate in the vessel center, forming a cylinder symmetric about the flow axis,[10,12,56] microfluidic experiments[20] and flow simulations[57,58] have shown that RBCs can lateralize within the capillary lumen. The lateralization causes RBCs to preferentially enter the downstream branch on the side where the larger fraction of their volume resides.[57] This effect becomes more prominent when two consecutive junctions are close, because the limited transit time between junctions restricts cells from migrating back to the flow centerline. Investigating the lateralization effect, however, requires precise measurements of the true anatomical lumen, which is beyond the scope of this study because of the low contrast of capillary walls.

Second, the clear departure of FQ_r values from the Pries model's predictions at the high and low ends of FQ_b values (Fig. 4A) may be related to differences in the tissues studied. As an extension of the brain, the retina differs fundamentally from mesenteric tissue in that its blood flow is tightly

Investigative Ophthalmology & Visual Science

coupled to neuronal activity.[4,5] The dynamic metabolic demands of retinal neurons in response to ambient visual stimuli likely require RBC flow to be redistributed in an efficient manner. The well-established spatial heterogeneity in retinal capillary blood flow[2,36] is thought to facilitate this process by acting as a functional reserve, allowing RBC flux to homogenize during periods of increased metabolic needs, which is predicted to enhance gas and metabolite exchange.[59] In this context, a less sigmoidal relationship between FQ_r and FQ_b would allow capillary junctions with highly imbalanced blood flow distributions at baseline (i.e., highly asymmetric FQ_b values) to redistribute RBC flow between the two branches more efficiently in response to increased neuronal activity. For such junctions, the same change in FQ_b would produce a greater change in FQ_r when the FQ_r versus FQ_b curve is less sigmoidal, owing to the steeper slopes at the tail ends. In contrast, a more sigmoidal FQ_r vs. FQ_b curve levels off more quickly toward its outer edges. Hence, capillary junctions with heavily skewed blood flow at baseline require larger changes in FQ_b to achieve comparable adjustments in FQ_r, reducing the efficiency of RBC flow redistribution.

Finally, differences in RBC rheology and experimental methods may also contribute to discrepancies in the reported RBC partitioning behavior. Compared with human RBCs, rat RBCs are smaller (~6 µm in diameter),[60] less deformable,[61,62] and less likely to aggregate into rouleaux,[62] all of which could influence cell distribution patterns at capillary bifurcations. Furthermore, the general anesthetics used for animal preparation in the Pries study[10] may have disrupted natural microvascular flow dynamics, given their known effects on vascular smooth muscle and endothelial cells.[63] In contrast, the non-invasive nature of the present study avoids such potential disruption and may give a more accurate representation of the natural state of capillary flow in the human retina.

Because there was no significant difference in fitting quality between the linear and logistic regressions, both the simplified Pries model (Equation 9) and the linear model (Equation 10) effectively describe RBC flow distribution at junctions presented in this study. Unlike the original Pries model,[10–12] neither of these models requires flow information from the main vessel. Because our observations were conducted on living human retinas, it was not possible to freely manipulate flow distribution through interventions such as clipping a downstream vessel,[10] making it difficult to directly measure the FQ_b threshold (i.e., the X_0 term in the Pries model) below which a branch vessel is completely deprived of cells. Our partitioning models are based on branch vessels with FQ_b values ranging from 0.14 to 0.86, which likely represent most single-file flow capillary junctions in a healthy retina, as the corresponding FQ_r range (0.06–0.96) already approaches the theoretical extremes of 0% and 100%. Extrapolating the linear model to $FQ_r = 0$ yields an FQ_b value of 0.127, suggesting that when fractional blood flow falls below 12.7%, a branch vessel may receive only plasma.

Limitations

The primary limitation of this study is that CFL thickness was not included in capillary lumen diameter estimates because of poor visibility. With the recently developed phase contrast imaging method,[48] it may be possible to generate significant noninvasive contrast for imaging the CFL; however, the limited numerical aperture of the human eye is likely to preclude accurate measurement of its thickness in narrow capillaries. Furthermore, the CFL is composed of a free-flowing region and a stagnant region bound to the glycocalyx,[64] with the latter not considered part of blood flow. Distinguishing between these two regions remains challenging without fluorescence labeling.[14,64] For the capillary junctions we analyzed, excluding the CFL from flow rate calculations still upheld blood flow conservation within ±20% across the junction. As such, measuring flow through the functional cell passage channel bound by the CFL appeared to be a simple yet effective approach for studying cell partitioning. Nonetheless, we acknowledge that neglecting the free-flowing CFL causes an underestimation of lumen diameter and an overestimation of hematocrit. Specifically, measuring hematocrit from the capillary lumen without considering the CFL produces estimates higher than the tube hematocrit (i.e., the fraction of the lumen occupied by RBCs) and closer to the discharge hematocrit (i.e., the fraction of the volumetric flow rate contributed by RBCs). The difference between tube and discharge hematocrit arises because flow in the CFL region is slower than in the RBC-occupied central region, making the CFL contribute less to the overall flow rate than its volumetric proportion in the capillary lumen suggests.[65]

Although cell-plasma fluid exchange provides a plausible interpretation of our results, confirming subtle RBC volume changes at femtoliter scale would ideally require imaging techniques with sub-micron resolution. It is well-established that RBCs exhibit complex features such as folding and membrane invagination in capillary flow.[66] Because of the lack of true 3D information, the pseudo-3D cell shapes derived from 2D images should be regarded as coarse approximations, prone to local errors in surface area and volume estimation. The resulting average cell representation, although useful for group-level analysis, does not capture the variability in individual RBC shapes and is influenced by the threshold used to segment the probability map. As such, it serves only as a statistical summary to facilitate relative comparisons of cell size between main and branch vessels, rather than providing absolute cell size measurements at sub-micron precision.

We note the average RBC volume of 74 fL and surface area of 91 µm^2 estimated in this study are lower than typical in vitro values (80 to 100 fL and ~130 µm^2).[67,68] This discrepancy may partly reflect the narrow capillaries sampled in our dataset (i.e., mean diameter ~4.6 µm), which likely restrict entry of larger RBCs. In our previous work using the same pseudo-3D reconstruction method in capillaries averaging ~5 µm in diameter, estimated cell volumes of 99 fL and surface areas of 110 µm^2 were more consistent with the physiological range reported in vitro.[25]

Individual variation in axial length and refractive error was not corrected for and may also introduce error into cell size estimates. However, since all three segments of each junction were captured within the same imaging field and thus subject to the same magnification effect, the fractional flow metrics used in our partitioning models, as well as the cell size comparisons between each pair of main and branch vessels, are expected to be robust. Furthermore, the simulation results in Supplementary Material S4 provide confidence that applying a consistent image processing pipeline across both vessel types does not introduce the kind of asymmetric bias that could explain the observed directional change in RBC volume.

Investigative Ophthalmology & Visual Science

The lingering of RBCs in the bifurcation region was not studied in depth, despite its documented influence on cell partitioning behavior in both computational flow simulations[17,57] and intravital observations.[13,26] Because of the transient nature of cell lingering,[17] quantifying its dynamic impact on cell partitioning requires unambiguous tracking of RBCs across junction points. This poses a challenge for noninvasive in vivo observations, as the close proximity of RBCs in the junction region complicates cell segmentation based on cell-plasma contrast, making it difficult to identify individual cell paths and measure their flow speed. Furthermore, multiple RBCs can linger simultaneously, obscuring whether a cell leaving the junction is the same one that entered moments earlier. Accurate tracking of individual cells across junctions would provide valuable insights for modeling RBC partitioning on a per-cell basis, factoring in flow speed, cell shape, and junction geometry to predict which branch a given RBC might enter at any given moment.

As is typical with noninvasive in vivo studies, we do not have direct control on basic flow parameters such as velocity and vessel diameter. Future investigations are needed to stress-test the models by, for example, exploring RBC flow redistribution resulting from flickering light stimulation[69,70] or from respiratory modulation of blood gases.[69]

Acknowledgments

Supported by an Australian Government Research Training Program Scholarship (YD) and Australian Research Council (DP240103352 to AM, PAB).

Disclosure: **Y. Ding**, None; **A.B. Metha**, None; **P. Bedggood**, None

References

1. Wong-Riley MT. Energy metabolism of the visual system. *Eye Brain*. 2010;2:99–116.
2. Yu D-Y, Cringle SJ, Paula KY, et al. Retinal capillary perfusion: spatial and temporal heterogeneity. *Prog Retin Eye Res*. 2019;70:23–54.
3. Bedggood P, Metha A. Direct visualization and characterization of erythrocyte flow in human retinal capillaries. *Biomed Opt Express*. 2012;3:3264–3277.
4. Alarcon-Martinez L, Villafranca-Baughman D, Quintero H, et al. Interpericyte tunnelling nanotubes regulate neurovascular coupling. *Nature*. 2020;585(7823):91–95.
5. Gonzales AL, Klug NR, Moshkforoush A, et al. Contractile pericytes determine the direction of blood flow at capillary junctions. *Proc Natl Acad Sci USA*. 2020;117:27022–27033.
6. Hartmann DA, Berthiaume AA, Grant RI, et al. Brain capillary pericytes exert a substantial but slow influence on blood flow. *Nat Neurosci*. 2021;24:633–645.
7. Fung Y. *Biodynamics: Circulation*. Berlin: Springer-Verlag; 1984.
8. Secomb TW, Pries AR. Blood viscosity in microvessels: experiment and theory. *C R Phys*. 2013;14:470–478.
9. Fahraeus R, Lindqvist T. The viscosity of the blood in narrow capillary tubes. *Am J Physiol Legacy Content*. 1931;96:562–568.
10. Pries AR, Ley K, Claassen M, Gaehtgens P. Red cell distribution at microvascular bifurcations. *Microvasc Res*. 1989;38:81–101.
11. Pries AR, Secomb TW, Gaehtgens P, Gross JF. Blood flow in microvascular networks. Experiments and simulation. *Circ Res*. 1990;67:826–834.
12. Pries AR, Reglin B, Secomb TW. Structural response of microcirculatory networks to changes in demand: information transfer by shear stress. *Am J Physiol Heart Circ Physiol*. 2003;284(6):H2204–2212.
13. Rashidi Y, Simionato G, Zhou Q, et al. Red blood cell lingering modulates hematocrit distribution in the microcirculation. *Biophys J*. 2023;122:1–12.
14. Vink H, Duling BR. Identification of distinct luminal domains for macromolecules, erythrocytes, and leukocytes within mammalian capillaries. *Circ Res*. 1996;79:581–589.
15. Balogh P, Bagchi P. The cell-free layer in simulated microvascular networks. *J Fluid Mech*. 2019;864:768–806.
16. Ebrahimi S, Balogh P, Bagchi P. Motion of a capsule in a curved tube. *J Fluid Mech*. 2021;907:A28.
17. Ebrahimi S, Bagchi P. A computational study of red blood cell deformability effect on hemodynamic alteration in capillary vessel networks. *Sci Rep*. 2022;12:1–19.
18. Balogh P, Bagchi P. Direct numerical simulation of cellular-scale blood flow in 3D microvascular networks. *Biophys J*. 2017;113:2815–2826.
19. Fallahi H, Zhang J, Phan HP, Nguyen NT. Flexible microfluidics: fundamentals, recent developments, and applications. *Micromachines*. 2019;10:830.
20. Mantegazza A, Clavica F, Obrist D. In vitro investigations of red blood cell phase separation in a complex microchannel network. *Biomicrofluidics*. 2020;14(1):014101.
21. Zhou Q, Fidalgo J, Bernabeu MO, Oliveira MSN, Krüger T. Emergent cell-free layer asymmetry and biased haematocrit partition in a biomimetic vascular network of successive bifurcations. *Soft Matter*. 2021;17:3619–3633.
22. Roman S, Merlo A, Duru P, Risso F, Lorthois S. Going beyond 20 µm-sized channels for studying red blood cell phase separation in microfluidic bifurcations. *Biomicrofluidics*. 2016;10(3):034103.
23. Sherwood JM, Holmes D, Kaliviotis E, Balabani S. Spatial distributions of red blood cells significantly alter local haemodynamics. *PLOS ONE*. 2014;9(6):e100473.
24. Jay AW. Viscoelastic properties of the human red blood cell membrane. I. Deformation, volume loss, and rupture of red cells in micropipettes. *Biophys J*. 1973;13:1166–1182.
25. Bedggood P, Ding Y, Metha A. Changes to the shape, orientation and packing of red cells as a function of retinal capillary size. *Biomed Opt Express*. 2024;15:558–578.
26. Kihm A, Quint S, Laschke MW, et al. Lingering dynamics in microvascular blood flow. *Biophys J*. 2021;120:432–439.
27. Schmid-Schönbein GW, Skalak R, Usami S, Chien S. Cell distribution in capillary networks. *Microvasc Res*. 1980;19:18–44.
28. Klitzman B, Johnson PC. Capillary network geometry and red cell distribution in hamster cremaster muscle. *Am J Physiology*. 1982;242(2):H211–H219.
29. Chui TYP, Mo S, Krawitz B, et al. Human retinal microvascular imaging using adaptive optics scanning light ophthalmoscopy. *Int J Retina Vitreous*. 2016;2:11.
30. Morgan JIW, Chui TYP, Grieve K. Twenty-five years of clinical applications using adaptive optics ophthalmoscopy [Invited]. *Biomedical Optics Express*. 2023;14:387–428.
31. Joseph A, Guevara-Torres A, Schallek J. Imaging single-cell blood flow in the smallest to largest vessels in the living retina. *eLife*. 2019;8:e45077.
32. Warner RL, Gast TJ, Sapoznik KA, Carmichael-Martins A, Burns SA. Measuring temporal and spatial variability of red blood cell velocity in human retinal vessels. *Invest Ophthalmol Vis Sci*. 2021;62(14):29.
33. Zhong Z, Song H, Chui TY, Petrig BL, Burns SA. Noninvasive measurements and analysis of blood velocity profiles in human retinal vessels. *Invest Ophthalmol Vis Sci*. 2011;52:4151–4157.

34. Bedggood P, Metha A. Mapping flow velocity in the human retinal capillary network with pixel intensity cross correlation. *PloS one*. 2019;14(6):e0218918.
35. Gu B, Wang X, Twa MD, Tam J, Girkin CA, Zhang Y. Noninvasive in vivo characterization of erythrocyte motion in human retinal capillaries using high-speed adaptive optics near-confocal imaging. *Biomed Opt Express*. 2018;9:3653–3677.
36. Neriyanuri S, Bedggood P, Symons RCA, Metha AB. Flow Heterogeneity and factors contributing to the variability in retinal capillary blood flow. *Invest Ophthalmol Vis Sci*. 2023;64(10):15.
37. Bedggood P, Ding Y, Metha A. Measuring red blood cell shape in the human retina. *Opt Lett*. 2023;48:1554–1557.
38. Delori FC, Webb RH, Sliney DH. Maximum permissible exposures for ocular safety (ANSI 2000), with emphasis on ophthalmic devices. *J Opt Soc Am A Opt Image Sci Vis*. 2007;24:1250–1265.
39. Bedggood P, Metha A. Analysis of contrast and motion signals generated by human blood constituents in capillary flow. *Opt Lett*. 2014;39:610–613.
40. Bedggood P, Metha A. Direct measurement of pulse wave propagation in capillaries of the human retina. *Opt Lett*. 2021;46:4450–4453.
41. Spangenberg P, Hagemann N, Squire A, et al. Rapid and fully automated blood vasculature analysis in 3D light-sheet image volumes of different organs. *Cell Rep Methods*. 2023;3(3):100436.
42. Fenton BM, Carr RT, Cokelet GR. Nonuniform red cell distribution in 20 to 100 micrometers bifurcations. *Microvasc Res*. 1985;29:103–126.
43. Bugliarello G, Hsiao GC. Phase separation in suspensions flowing through bifurcations: a simplified hemodynamic model. *Science*. 1964;143(3605):469–471.
44. Barber JO, Alberding JP, Restrepo JM, Secomb TW. Simulated two-dimensional red blood cell motion, deformation, and partitioning in microvessel bifurcations. *Ann Biomed Eng*. 2008;36:1690–1698.
45. Wang T, Rongin U, Xing Z. A micro-scale simulation of red blood cell passage through symmetric and asymmetric bifurcated vessels. *Sci Rep*. 2016;6(1):20262.
46. Jay AW. Viscoelastic properties of the human red blood cell membrane. I. Deformation, volume loss, and rupture of red cells in micropipettes. *Biophys J*. 1973;13:1166–1182.
47. Gu Y, Oliferenko S. The principles of cellular geometry scaling. *Curr Opin Cell Biol*. 2021;68:20–27.
48. Bedggood P, Ding Y, Dierickx D, Dubra A, Metha A. Quantification of optical lensing by cellular structures in the living human eye. *Biomed Opt Express*. 2025;16:473–498.
49. Danese E, Lippi G, Montagnana M. Red blood cell distribution width and cardiovascular diseases. *J Thorac Dis*. 2015;7(10):E402–E411.
50. Coin JT, Olson JS. The rate of oxygen uptake by human red blood cells. *J Biol Chem*. 1979;254:1178–1190.
51. Richardson SL, Hulikova A, Proven M, et al. Single-cell O(2) exchange imaging shows that cytoplasmic diffusion is a dominant barrier to efficient gas transport in red blood cells. *Proc Natl Acad Sci USA*. 2020;117:10067–10078.
52. Benga G. The first discovered water channel protein, later called aquaporin 1: Molecular characteristics, functions and medical implications. *Mol Aspects Med*. 2012;33:518–534.
53. Sugie J, Intaglietta M, Sung LA. Water transport and homeostasis as a major function of erythrocytes. *Am J Physiol Heart Circ Physiol*. 2018;314(5):H1098–H1107.
54. Fung Y-C. *Biomechanics: mechanical properties of living tissues*. Berlin: Springer Science & Business Media; 2013.
55. Krogh A. Studies on the physiology of capillaries: II. The reactions to local stimuli of the blood-vessels in the skin and web of the frog. *J Physiol*. 1921;55(5-6):412–422.
56. Haynes RH. Physical basis of the dependence of blood viscosity on tube radius. *Am J Physiol*. 1960;198:1193–1200.
57. Balogh P, Bagchi P. Analysis of red blood cell partitioning at bifurcations in simulated microvascular networks. *Phys Fluids*. 2018;30(5):051902.
58. Zhou Q, Perovic T, Fechner I, et al. Association between erythrocyte dynamics and vessel remodelling in developmental vascular networks. *J R Soc Interface*. 2021;18(179):20210113.
59. Jespersen SN, Østergaard L. The roles of cerebral blood flow, capillary transit time heterogeneity, and oxygen tension in brain oxygenation and metabolism. *J Cereb Blood Flow Metab*. 2012;32:264–277.
60. Straat M, Klei TRL, de Korte D, van Bruggen R, Juffermans NP. Accelerated clearance of human red blood cells in a rat transfusion model. *Intensive Care Med Exp*. 2015;3:27.
61. Baskurt OK. Deformability of red blood cells from different species studied by resistive pulse shape analysis technique. *Biorheology*. 1996;33:169–179.
62. da SilveiraCavalcante L, Acker JP, Holovati JL. Differences in rat and human erythrocytes following blood component manufacturing: the effect of additive solutions. *Transfus Med Hemother*. 2015;42:150–157.
63. Akata T, Warltier David C. General anesthetics and vascular smooth muscle: direct actions of general anesthetics on cellular mechanisms regulating vascular tone. *Anesthesiology*. 2007;106:365–391.
64. Pries AR, Secomb TW, Gaehtgens P. The endothelial surface layer. *Pflugers Arch*. 2000;440:653–666.
65. Botkin ND, Kovtanyuk AE, Turova VL, Sidorenko IN, Lampe R. Accounting for tube hematocrit in modeling of blood flow in cerebral capillary networks. *Comput Math Methods Med*. 2019;2019:4235937.
66. Takeishi N, Imai Y. Capture of microparticles by bolus flow of red blood cells in capillaries. *Sci Rep*. 2017;7(1):5381.
67. Fung Y-C. Stochastic flow in capillary blood vessels. *Microvasc Res*. 1973;5:34–48.
68. Canham PB, Burton AC. Distribution of size and shape in populations of normal human red cells. *Circ Res*. 1968;22:405–422.
69. Duan A, Bedggood PA, Metha AB, Bui BV. Reactivity in the human retinal microvasculature measured during acute gas breathing provocations. *Sci Rep*. 2017;7(1):2113.
70. Warner RL, de Castro A, Sawides L, et al. Full-field flicker evoked changes in parafoveal retinal blood flow. *Sci Rep*. 2020;10(1):16051.

Investigative Ophthalmology & Visual Science